

# Numerical computation of the sensitivity kernel for monitoring weak changes with multiply scattered acoustic waves

Chinaemerem Kanu and Roel Snieder

*Center for wave phenomena, Colorado School of Mines, Golden, CO 80401, USA. E-mail: ckanu@mines.edu*

Accepted 2015 September 14. Received 2015 September 11; in original form 2015 January 2

## SUMMARY

Monitoring of weak localized changes within a medium using coda waves, we can either use the decorrelation and/or the phase shift of the coda waves. The formulation for both the decorrelation and the phase shift of the coda waves due to weak changes contain a common sensitivity kernel that is needed to image the weak localized changes. We provide a novel approach to compute the sensitivity kernel which uses finite difference modelling of the wavefields from the source and the receiver with an *a priori* scattering model. These wavefields give the intensities needed to compute the sensitivity kernels. This approach unlike methods that computes the sensitivity kernel with analytical approximations of the scattered intensity computes the numerical solution of the scattered intensity with a prior scattering model. The numerical solution of the sensitivity kernel allows us to use an arbitrary earth model that includes a free surface without simplifying the property of the scattering model. We demonstrate the computation of the numerical sensitivity kernel within statistically heterogeneous models and models with irregular topography. The statistically heterogeneous models we explore include a simple model for vertically fractured and horizontally layered shale reservoirs. We compare the impact of either the horizontal or the vertical source–receiver configuration on the characteristics of the sensitivity kernel. All computations of the numerical kernel we present in this study use 2-D heterogeneous scattering models, however, the kernel computation is easily extended to 3-D scattering models.

**Key words:** Numerical solutions; Interferometry; Seismic tomography.

## 1 INTRODUCTION

Multiple scattering of seismic waves potentially provides information about the subsurface that can be used to increase the resolution of an imaged subsurface with multiple reflected waves (Belkebir *et al.* 2006), increase illumination especially within a poorly illuminated subsurface (Gaburro *et al.* 2007; Fleury 2013) and monitor weak time-lapse changes within the earth's subsurface (Poupinet *et al.* 1984; Snieder *et al.* 2002; Schaff & Beroza 2004). Using scattered waves, especially for monitoring weak changes within the subsurface, we can increase the illumination and sensitivity to changes within a subsurface (Malcolm *et al.* 2009; Berkhout *et al.* 2012). Multiply scattered waves are used for monitoring weak changes such as velocity changes as weak as 0.1 per cent (Snieder 2002) and monitoring defects within mechanical structures (Masera *et al.* 2011) that can be detected with waveform changes. These weak changes within the earth's subsurface (both natural and induced) are usually either gradual, weak, or localized both in space and time. Detecting these changes in many cases requires data that are highly sensitive to the changes. Vlastos *et al.* (2006) show that the sensitivity of multiply scattered waves to weak changes is significantly higher than the sensitivity of the ballistic or direct part of the

seismic waves to weak changes. This increase in the sensitivity is due to the repeated sampling of the weak velocity changes by the scattered waves (Snieder *et al.* 2002; Rossetto *et al.* 2011). The high sensitivity of the multiply scattered waves has led to successful detection of time-lapse velocity changes within the earth's subsurface. Poupinet *et al.* (1984) use coda waves generated by repeating earthquakes to observe an average *S* wave velocity change of 0.2 per cent after the 1979  $M_w$  5.9 Coyote Lake earthquake on the Calaveras Fault, California. Using cross-correlation functions generated from seismic noise, Wegler & Sens-Schönfelder (2007) detect a sudden decrease in the seismic velocity of the region surrounding the 2004  $M_w$  6.6 Mid-Niigata earthquake rupture. Using controlled-source monitoring Nishimura *et al.* (2000) detected a velocity decrease of 0.3–1.0 per cent due to the 1998  $M_w$  6.1 Mount Iwate earthquake. However, Pacheco & Snieder (2005) show that the spatial sensitivity of the multiply scattered waves to the weak changes is not uniformly distributed but is dependent on the source and receiver locations, on the position of the weak changes, on the scattering medium and on the coda traveltime.

Most monitoring of weak changes within the earth's subsurface using multiply scattered (coda) waves has been limited to identifying weak changes rather than localizing these changes.

Except in very densely distributed source and receiver configurations, the velocity changes detected by coda wave interferometry are spatially averaged velocity changes. Recently, successful efforts have been made not only in identifying the weak changes using multiply scattered waves, but also in localizing the changes in a statistically homogeneous scattering medium (Rossetto *et al.* 2011; Obermann *et al.* 2013a; Planès *et al.* 2014). However, to localize changes within the earth's subsurface - a scattering medium which is most likely to be inhomogeneous—we will need to appropriately handle the inhomogeneities of the earth's subsurface. Because of the prominence of surface waves, we also need to account for the presence of a free surface.

The complexity in the travel paths of the multiply scattered waves, which depends on the scattering properties of the medium of interest, makes it challenging to accurately describe the origin, travel paths and distribution of the scattered waves within the medium. In a strongly scattering medium, the multiply scattered waves for late lapse time can be described as a diffusive process (Wesley 1965; Shapiro & Kneib 1993; Page *et al.* 1995). The diffusion model has been used successfully in imaging algorithms that use multiply scattered waves in medical imaging (Yodh & Chance 1995) or in imaging of missing scatterers (Rossetto *et al.* 2011). But, the validity of using the diffusion intensity model in explaining the multiple scattering of waves depends on the strength of the scattering process. Even in a strongly scattering medium, the diffusion intensity model is only accurate at large lapse times, that is, for  $t \gg r/c$ , where  $t$  is the traveltime,  $r$  is the source–receiver distance and  $c$  is the average velocity of the medium. Alternatively, the scattered intensity can be modelled using the radiative transfer intensity model, which more accurately predicts the scattered intensity for all scattering regimes (Paasschens 1997; Turner & Weaver 1994). The diffusion and radiative transfer intensity models, however, are analytical models developed under the assumption of a stochastic wave equation. These analytical intensity models, as well as most other intensity models for the scattered waves, are based on homogeneous or simple scattering media. The scattered intensity is, however, affected by statistical changes in the scattering properties, as well as by the presence of a free surface. We show that for more realistic media, the scattered intensity of the medium can be modelled numerically using, for example, finite-difference modelling rather than using the analytical intensity models.

In this study, we explore the capability of computing the sensitivity kernel that we need for monitoring and localizing the weak changes within a medium. In the next section, we describe the theoretical connection of the sensitivity kernel to the estimated time-shifts or the decorrelations in the time lapse and perturbed scattered waves resulting from the weak changes. In Section 3, we develop a novel approach for computing the kernel numerically for any scattering model and explore the behaviour of the kernel using various sample scattering models. In Section 4, we discuss the practicality of the kernel computation.

## 2 SENSITIVITY KERNEL

Imaging weak velocity changes in random scattering media with multiply scattered waves requires characterizing the distribution and origin of the used scattered waves. Pacheco & Snieder (2005) use the intensity of multiply scattered waves to develop a sensitivity kernel  $K(\mathbf{s}, \mathbf{x}_0, \mathbf{r}, t)$  which relates the mean traveltime changes  $\langle \tau \rangle$  to the localized relative velocity change  $\delta v/v(\mathbf{x}_0)$  within the

subsurface:

$$\langle \tau(t) \rangle = - \int_V K(\mathbf{s}, \mathbf{x}_0, \mathbf{r}, t) \frac{\delta v}{v}(\mathbf{x}_0) dV(\mathbf{x}_0), \quad (1)$$

where  $t$  is the traveltime of the scattered wave,  $V$  is the scattering volume, and  $\mathbf{s}$  and  $\mathbf{r}$  are the source and the receiver locations, respectively. The sensitivity kernel  $K(\mathbf{s}, \mathbf{x}_0, \mathbf{r}, t)$  provides a link between the estimated traveltime changes with the fractional velocity change transversed by the scattered waves. The sensitivity kernel depends on the source and receiver locations, the scattering property of the medium, and the traveltime of the scattered wave.

Rossetto *et al.* (2011) consider a different problem where the local scattering strength changes. This change is accounted for by a change in scattering cross-section  $\delta\sigma(\mathbf{x}_0)$  within the scattering medium. Using the correlation function  $C(\mathbf{s}, \mathbf{r}, t)$  of the multiply scattered waves in a medium with this time-lapse change, they relate the decorrelation  $1 - C(\mathbf{s}, \mathbf{r}, t)$  between the perturbed and unperturbed scattered waves to the weak change in the total scattering cross-section of the medium:

$$1 - C(\mathbf{s}, \mathbf{r}, t) = \int_V \frac{v(\mathbf{x}_0)\delta\sigma(\mathbf{x}_0)}{2} K(\mathbf{s}, \mathbf{x}_0, \mathbf{r}, t) dV(\mathbf{x}_0). \quad (2)$$

Using either the time-shifts or the decorrelation values from the time-lapse multiply scattered waves for resolving localized weak changes, the sensitivity kernel  $K(\mathbf{s}, \mathbf{x}_0, \mathbf{r}, t)$  forms the building block for the Fréchet derivatives needed to resolve the weak changes. The sensitivity kernel  $K(\mathbf{s}, \mathbf{x}_0, \mathbf{r}, t)$  is given by

$$K(\mathbf{s}, \mathbf{x}_0, \mathbf{r}, t) = \frac{\int_0^t P(\mathbf{s}, \mathbf{x}_0, t')P(\mathbf{x}_0, \mathbf{r}, t - t') dt'}{P(\mathbf{s}, \mathbf{r}, t)}, \quad (3)$$

where  $P$  is the normalized intensity of the multiply scattered waves (Pacheco & Snieder 2005). The normalized intensity can be computed using different methods. The normalized intensity in a homogeneous scattering medium in the diffusion approximation is given by (Paasschens 1997):

$$P(\mathbf{s}, \mathbf{r}, t) = \frac{1}{(4\pi Dt)^{d/2}} \exp\left(-\frac{R_{sr}^2}{4Dt}\right), \quad (4)$$

where  $d$  is the dimension of the scattering medium,  $R_{sr} = |\mathbf{r} - \mathbf{s}|$  is the source–receiver distance and  $D$  is the diffusion coefficient. The normalized intensity can also be described by the radiative transfer model. The 2-D radiative transfer intensity (Paasschens 1997) is

$$P(\mathbf{s}, \mathbf{r}, t) = \frac{\exp(-vt/l)}{2\pi R_{sr}} \delta(vt - R_{sr}) + \frac{1}{2\pi lvt} (1 - R_{sr}^2/v^2t^2)^{-1/2} \times \exp(\sqrt{v^2t^2 - R_{sr}^2}/l - vt)\Theta(vt - R_{sr}), \quad (5)$$

where  $l$  is the scattering mean free path;  $\delta$  and  $\Theta$  are the Dirac delta and the Heaviside step functions, respectively.

The above models of the scattered intensity assume that the statistical properties of the medium fluctuations are homogeneous. The assumption of statistical homogeneity is not realistic for the Earth, where the scattering properties change with depth or laterally. Complex heterogeneous models and arbitrary boundary conditions require a more complex mathematical model to describe the intensity of the scattered waves (Margerin & Sato 2011). These complex heterogeneous media include heterogeneously layered media (Margerin *et al.* 1998; Haney *et al.* 2005) and media with non-diffusive regions (Ripoll *et al.* 2001). In addition, one may also need to account for the presence of a free surface. To avoid the assumption of statistical homogeneity, we compute the normalized

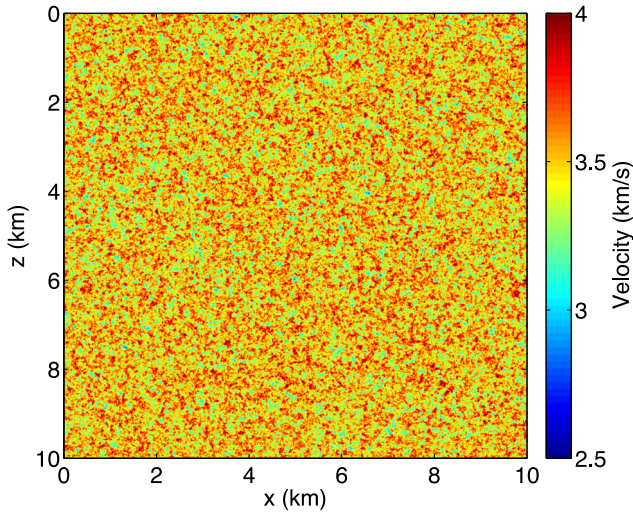


Figure 1. Velocity model for numerical computation of sensitivity kernel for comparison with the analytical solution.

intensity by numerically simulating the waves propagating through a number of realizations of the scattering medium, and compute the intensity from these waveforms. The numerically generated scattered intensity takes the variations of the statistical properties of the medium fluctuations into account, as well as the presence of a free surface.

### 3 NUMERICAL COMPUTATION OF SENSITIVITY KERNEL

For most scattering media, especially for complex heterogeneous scattering media, the sensitivity kernel  $K(\mathbf{s}, \mathbf{x}_o, \mathbf{r}, t)$  can be computed numerically. For these scattering media, an exact analytical formulation for either the intensity of the scattered waves or the corresponding sensitivity kernel for imaging the weak changes are usually not available. Using eq. (3) and a model of the scattering medium, we can numerically compute the sensitivity kernel by simulating the scattered wavefield with the scattering model, then compute the intensity field from the simulated wavefield. However, the numerical computation of the sensitivity kernel depends on how well one knows the statistical properties of the scattering medium. The requirement of the statistical properties of the scattering medium use for the kernel estimation is that the statistical properties explain the recorded scattered intensities (Pacheco & Snieder 2005). The characteristics of the heterogeneous medium, such as the scattering mean free path length and the average velocity, can be estimated from the analysis of the coda waves in recorded data (Sato *et al.* 2012; Obermann *et al.* 2013b) or using additional information such as velocity values from well log measurements when available or a velocity model obtained from other geophysical methods.

We compute the sensitivity kernel using eq. (3). We generate the source and the receiver wavefields by numerical computation of waves excited at the source and receiver locations, respectively. Here, we use acoustic modelling. We also use absorbing boundary conditions at the boundaries of our models. We do not include a

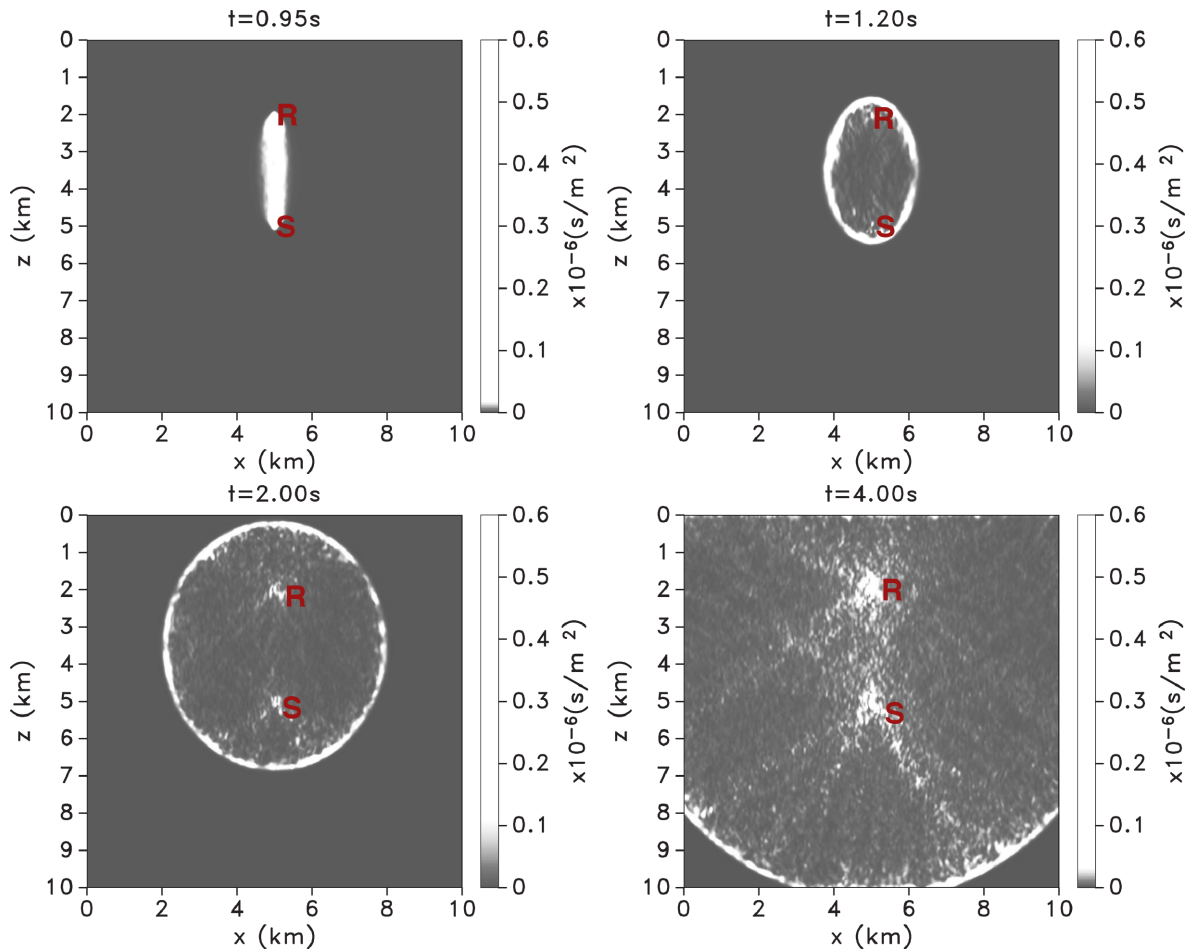


Figure 2. Temporal and spatial evolution of the sensitivity kernel (numerical solution).

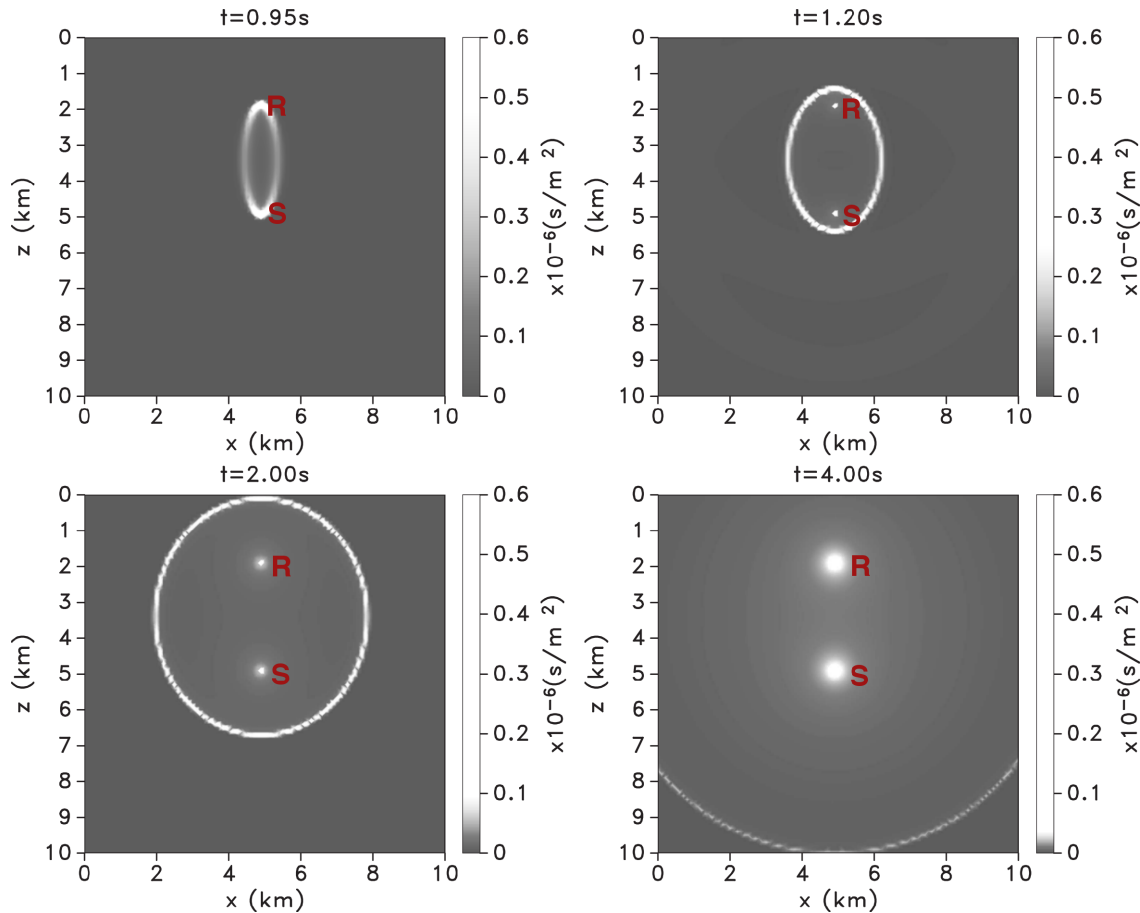


Figure 3. Temporal and spatial evolution of the sensitivity kernel using the radiative transfer model.

free-surface boundary condition except for the model with variable topography (section 3.3). The normalized intensities are the square of the envelope of the generated wavefields normalized by the spatial integral of the intensity  $\int_V P(\mathbf{x}_0, t) dV(\mathbf{x}_0)$  (Sato *et al.* 2012). The normalization of the scattered intensity removes imprints of the source time function from the acoustic intensity field. To compute the sensitivity kernel  $K(\mathbf{s}, \mathbf{x}_0, \mathbf{r}, t)$ , we convolve the source and the receiver intensity fields and normalize with the denominator in eq. (3). We simulate the wavefields with finite difference modelling using a realization of a von-Karman random velocity model (Sato *et al.* 2012). The 2-D von-Karman power spectral density function (PSDF)  $\tilde{P}_{2D}$  is given by

$$\tilde{P}_{2D}(k_x, k_z) = \frac{4\pi\Gamma(\kappa + 1)\epsilon^2\sqrt{a_x^2 + a_z^2}}{\Gamma(\kappa)\left(1 + [k_x^2 a_x^2 + k_z^2 a_z^2]\right)^{\kappa+1}}, \quad (6)$$

where  $\kappa$  is the von-Karman exponent,  $\epsilon$  is the fluctuation strength of the scattering model,  $a_x$  and  $a_z$  are the correlation lengths along the  $x$ - and  $z$ -directions, respectively, and  $k_x$  and  $k_z$  are the wavenumbers along the  $x$ - and  $z$ -directions, respectively. The correlation length is  $a = \sqrt{a_x^2 + a_z^2}$ . A wide range of values have been associated with the von-Karman parameters for the earth subsurface. The values of the von-Karman parameters depend on the subsurface lithology and depth. Yoshimoto & Sato (1997), using 149 waveforms in the frequency band of 8–16 Hz from 10 earthquakes occurring at depths shallower than 10 km, estimate the range of  $\epsilon$  and  $a$  values to be 5–8 per cent and 0.3–0.8 km, respectively, in the Nilko area of Japan. We use the von-Karman scattering model in order to generate a

variety of scattering models with earth-like parameter values solely for the numerical test of the kernel computation (Sato *et al.* 2012). The examples shown can be generalized for any statistical model for the medium fluctuations.

The scattering model we use for kernel computation consists of the random velocity fluctuations defined by the von-Karman parameters and constant density. One could take fluctuations in the density into account as well, but for simplicity we perturbed only the velocity. The velocity model is given by

$$v(\mathbf{x}) = v_0(\mathbf{x})[1 + \zeta(\mathbf{x})], \quad (7)$$

where  $v_0(\mathbf{x})$  is the background velocity and  $\zeta(\mathbf{x})$  is a realization of the random velocity fluctuation for the von-Karman PSDF in eq. (6) (Sato *et al.* 2012).

### 3.1 Numerical versus analytical computation

The sensitivity kernel can be estimated from analytical models of the scattered intensity (the diffusion and radiative transfer approximation of the scattered intensity). To compare the analytical and numerical solution of the sensitivity kernel, we use a von-Karman scattering model defined by the following parameters:  $a_x = a_y = 0.01$  km,  $\epsilon = 0.1$ ,  $\kappa = 0.5$ , and  $f = 15$  Hz ( $\lambda = 0.23$  km). This scattering model and the dominant scattering wavenumber correspond to  $ka \simeq 0.27$ . The scattering velocity model is given in Fig. 1 with an average velocity of  $3.5$  km s<sup>-1</sup>. The theoretical scattering ( $l_{VK}$ ) and transport ( $l_{VK}^*$ ) mean free path lengths for these von-Karman parameters and the scattered waves are 5.7 km and 6.9 km,

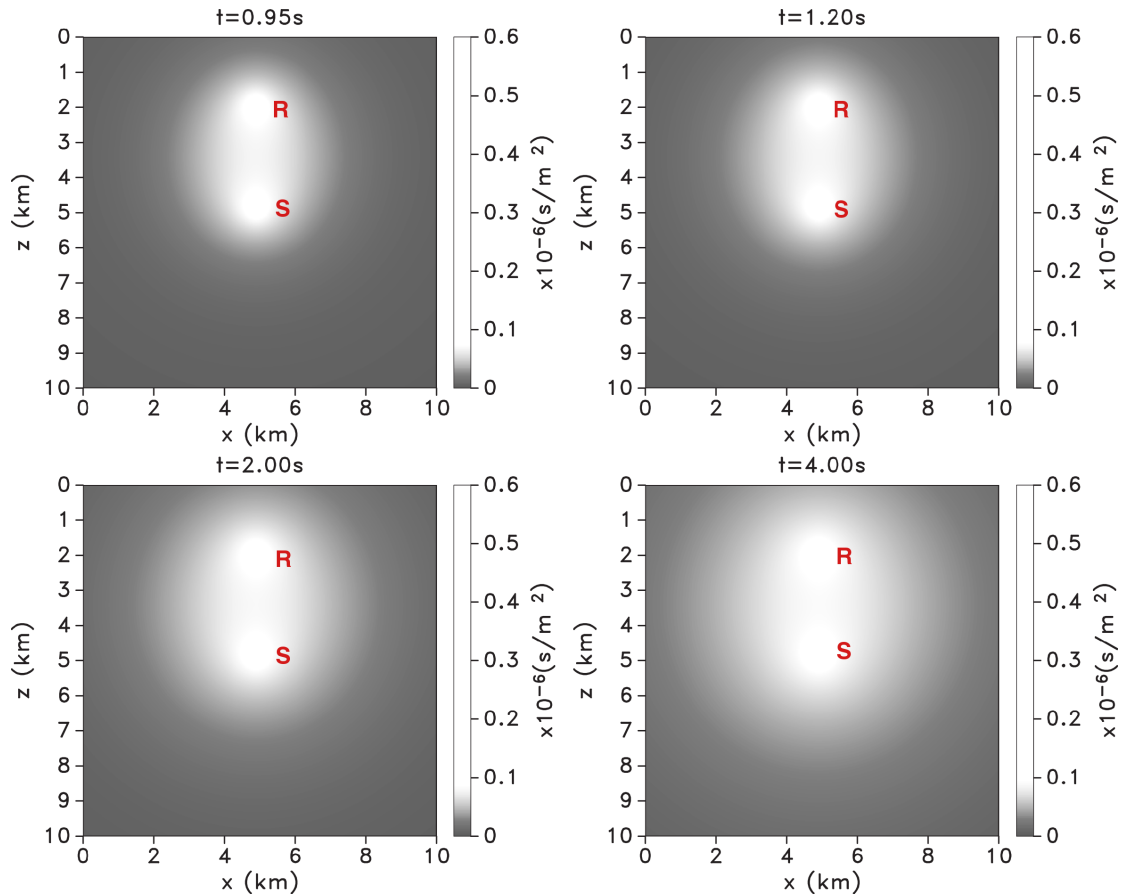


**Figure 4.** Temporal and spatial evolution of the sensitivity kernel using the diffusion model.

respectively (Sato *et al.* 2012). These scattering parameters, however, are not used for the computation of the numerical sensitivity kernels.

We compute the analytical solution of the sensitivity kernel using the corresponding theoretical mean free path lengths and the approximations of the scattered intensity using the diffusion (eq. 4) and the radiative transfer (eq. 5) models. We also convolve the analytical intensities with the intensity of the source wavelet used for the computation of the numerical kernel. Figs 2–4 show time snapshots 0.95, 1.20, 2.00 and 4.00 s of the sensitivity kernel for both the numerical and the analytical solutions, respectively. The numerical solution of the sensitivity kernel is bound by a kernel front which is defined as the edge of the kernel that is composed of single scattering and bounds the multiple scattering contributions. The numerical sensitivity kernel shows similar features represented in the radiative transfer model (Fig. 3) of the sensitivity kernel including the direct line-of-sight characteristic of the ballistic kernel (0.95 s) and the elliptical shape of the kernel front at lapse times after the first arrival time. The major difference between the numerical kernel and the radiative transfer kernel is the fluctuations in the numerical kernel. The numerical kernel in Fig. 2 is computed with one realization of the scattering model. The diffusion approximation of the sensitivity kernel (Fig. 4), as expected, only reproduces the spatial features of the kernel at long lapse times ( $ct/R_{sr} \gg 1$ ) (Paasschens 1997) with no clear ellipsoidal edge. Fig. 5 shows a cross-section of the kernel along the source–receiver line. The diffusion kernel fails to explain the zero or near-zero sensitivity of the kernel beyond the kernel front, evident in both the numerical and the radiative transfer kernels.

The spatial and temporal behaviour of the kernel implies that to resolve weak changes within a scattering medium with homogeneous statistical properties, the radiative transfer kernel is close to the numerical kernel solution. However, the similarity between the radiative transfer kernel and the numerical kernel breaks down within statistically heterogeneous media and in the presence of variable topography because of the homogeneity of the radiative transfer model (Paasschens 1997; Turner & Weaver 1994). Fig. 5 shows that the numerical kernel has more fluctuations compared to the analytical solutions. This numerical kernel is computed with one realization of the scattering model. The fluctuations in the kernel are due to the details in the fluctuations of the used realization of the scattering model. We can suppress these fluctuations by averaging the kernel over a number of the realizations of the scattering model with the same statistical properties. Fig. 6 shows the averaged kernel at traveltime 2.00 s over 1, 5, 10 and 20 realizations of the scattering model. Increasing the number of realizations of the model used for the kernel computation reduces the fluctuations both at the singly scattered and multiply scattered part of the kernel. With few realizations of the random model (five realizations) we can achieve stability in the sensitivity kernel (Fig. 7).

## 3.2 Scattering velocity models

### 3.2.1 Random isotropic scattering model

Fig. 2 shows the kernel for a given source–receiver pair (S–R) at the following time snapshots: 0.95, 1.20, 2.00 and 4.00 s. The direct wave excited by a source S arrives at the receiver R at traveltime

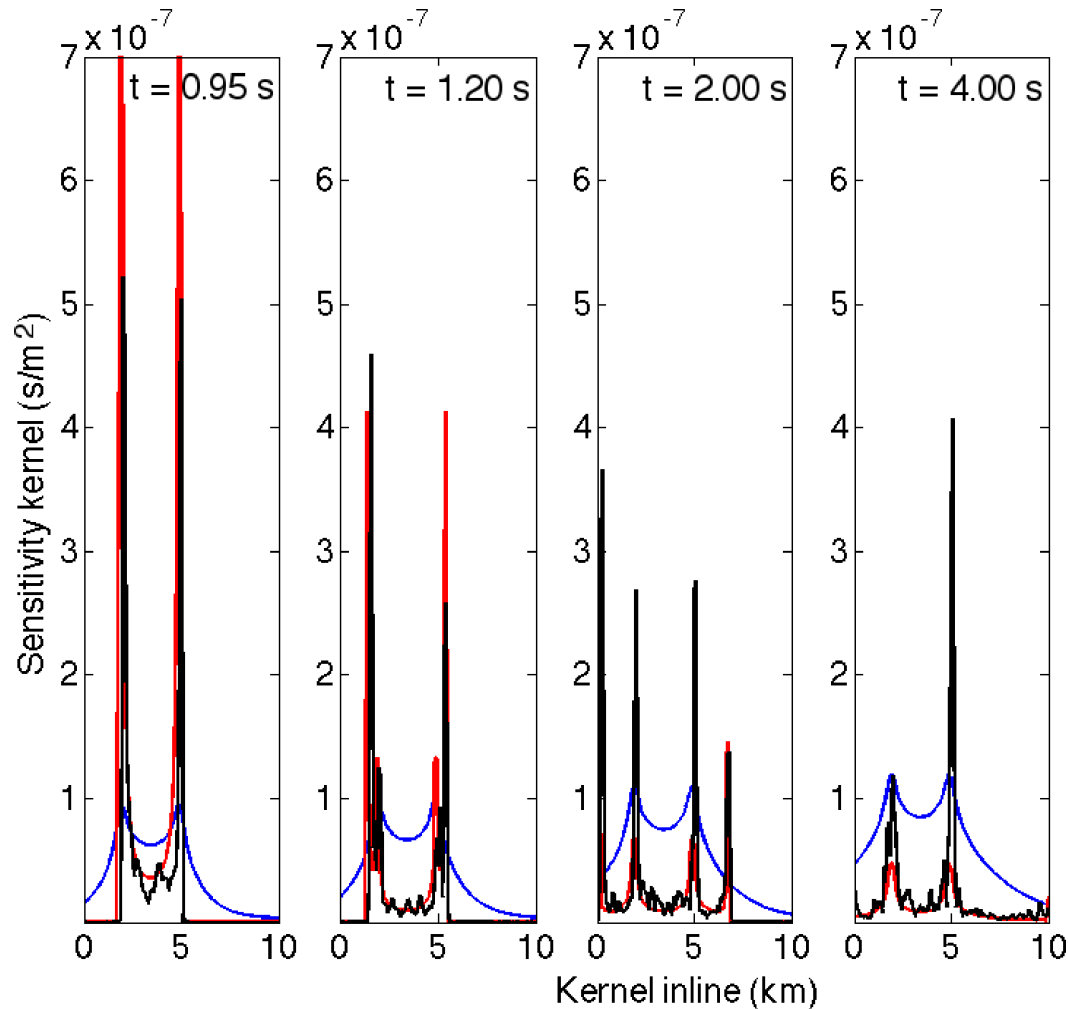


**Figure 5.** Comparison between numerical sensitivity kernel (black line) and diffusion-based (blue line) and radiative transfer-based (red line) kernel along the source (at 2 km) receiver (at 5 km) line.

$t = 0.90$  s with an average velocity of  $3.5 \text{ km s}^{-1}$ . The time snapshots of the kernel shown in Fig. 2 show the sensitivity to the changes in the scattering model for the scattered phases arriving at a specific traveltime  $t$ . The kernel at  $t = 0.95$  s corresponds to the sensitivity of scattered waves dominated by direct and forward scattered waves. With increasing time, the area covered by the sensitivity kernel progressively increases. The spatial broadening of the kernel with time increases the detectability of any change in the scattering property of the medium due to multiple interaction between the scattered waves and the change, especially changes away from the path of the direct wave (which is along the source–receiver line in this case). However, the resolving power of the kernel is expected to decrease with increasing time because of the spatial broadening of the kernel. The shape of the kernel with increasing time depends on the source and receiver locations, the corresponding traveltime, and the properties of the scattering medium. At times  $t > 0.95$  s, the kernel assumes an elliptical shape with the major axes along the source–receiver line and the minor axes perpendicular to the source–receiver line. The edge of the kernel is dominated by contributions from single scattering. The kernel for the singly scattered waves is given by (Pacheco & Snieder 2006)

$$K(\mathbf{x}_0, t) = \frac{1}{2\pi h \sqrt{(ct/R_{sr} - 1)}} \left[ \frac{r_s}{s} + \frac{r_r}{r} \right], \quad (8)$$

where  $s$  and  $r$  are the distances from the point  $\mathbf{x}_0$  to the source and receiver, respectively;  $r_s$  and  $r_r$  are the distances from any point on the kernel front to the source and receiver, respectively.

The single-scattering-dominated part of the kernel spatially bounds the multiple scattering part of the kernel. The inner part of the kernel accounts for multiple scattering, which has lower amplitude compared to the kernel contribution from the single scattering. Within the multiple-scattering-dominated part of the kernel, there are high sensitivities at the source and receiver locations which are predicted accurately by the analytical solutions in Fig. 5. These high sensitivities at or near the source and receiver locations suggest that the dominant contribution to the multiply scattered waves recorded at receiver R due to a source S originates from scattering near the source and receiver locations.

### 3.2.2 Random non-isotropic scattering model

The scattering properties within the earth's subsurface are generally complex and inhomogeneous. The scattering characteristics of the subsurface can vary from place to place depending on both the underlying lithology and overlaying stress conditions of the local and regional subsurface. The scattering properties of the earth's subsurface also vary with depth (Shearer & Earle 2008). The stress- and

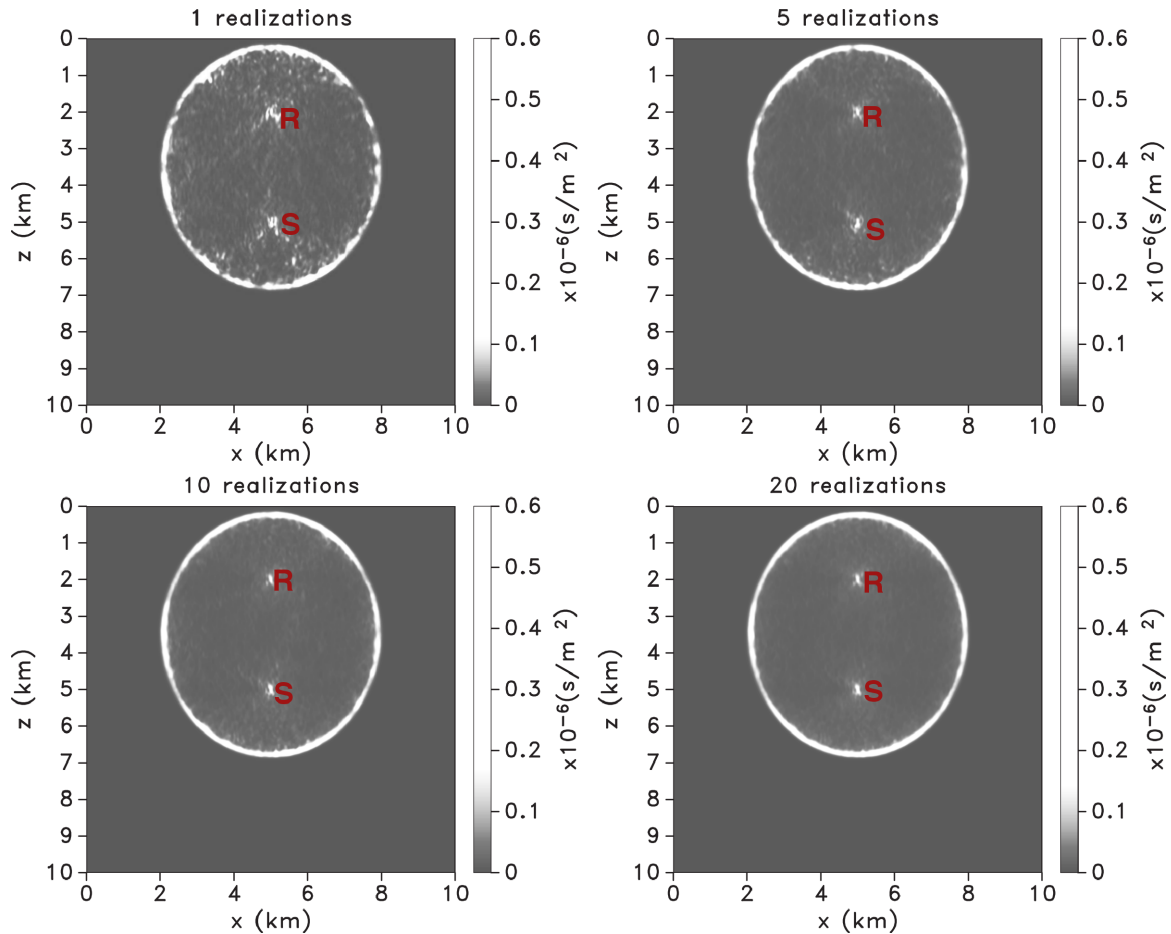


**Figure 6.** Comparison of the kernel at  $t = 2.0$  s using a number of scattering model realizations.

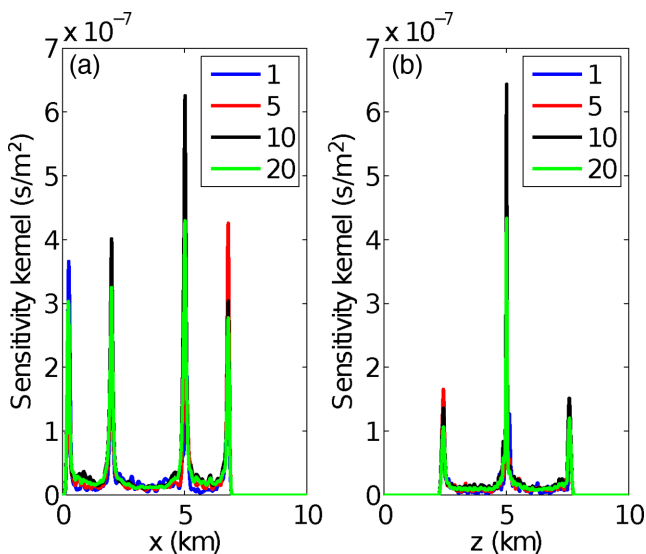


**Figure 7.** The inline section (a) and the crossline section (b) of the kernel at  $t = 2.0$  s after averaging over 1, 5, 10 and 20 realizations of the scattering model with the same statistical properties.

depth-dependent scattering properties of the subsurface controls the scattering process of the seismic wave travelling through the subsurface. The effective scattering of the subsurface are defined by both the scattering properties of the subsurface and the characteristics

of the incident seismic phase that is scattered. The characteristics of the incident phase include the incidence angle of the wave, the spectral properties of the incident wave, and the wave mode of the incident wave (Levander 1990).

To explore the dependence of the sensitivity kernel on the scattering medium, we test two scattering models whose background velocity is a 3-layered velocity model. In both models (Fig. 8), the top and bottom layers have the same scattering properties given by the von-Karman PSDF. For the top layer,  $\kappa = 0.5$ ,  $\epsilon = 0.5$ , and  $a_z = a_x = 0.05$  km; for the bottom layer,  $\kappa = 0.8$ ,  $\epsilon = 0.1$ , and  $a_z = a_x = 0.1$  km. However, in the middle layer, one model consists of vertical velocity perturbations while the other model is composed of horizontal velocity perturbations. The model with vertical velocity perturbations mimics a highly vertically fractured reservoir while the model with horizontal velocity perturbations represents a shale-like reservoir with a thin laminated layering. The middle layer for both models is defined by the following von-Karman parameters. For the vertically fractured model,  $a_z = 0.5$  km and  $a_x = 0.0001$  km; for the shale-like model,  $a_z = 0.0001$  km and  $a_x = 0.5$  km. In both scattering models,  $\kappa = 0.1$  and  $\epsilon = 0.5$  for the middle layer. In both scattering models, we compute the sensitivity kernels using two source–receiver configurations. In one configuration, the source–receiver line is vertical (Figs 9 and 11) while in the second configuration the source–receiver line is horizontal (Figs 10 and 12) and is embedded within the middle layer. These source–receiver configurations resemble a source such as a microseismic event or an earthquake embedded within the subsurface with either

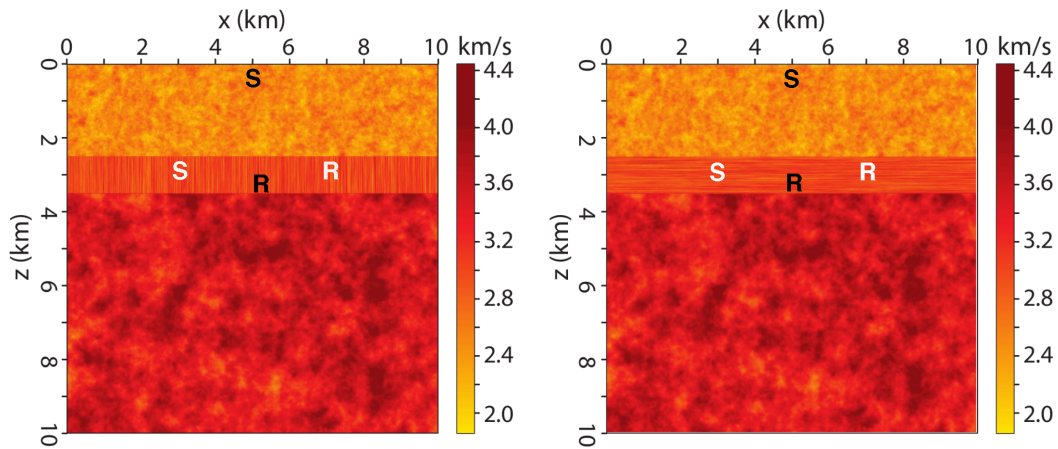


**Figure 8.** Left: velocity model with a vertical-fractured-like reservoir, and Right: velocity model with a shale-like reservoir. The vertical and the horizontal source–receiver configurations are given by the black and white S and R locations, respectively.

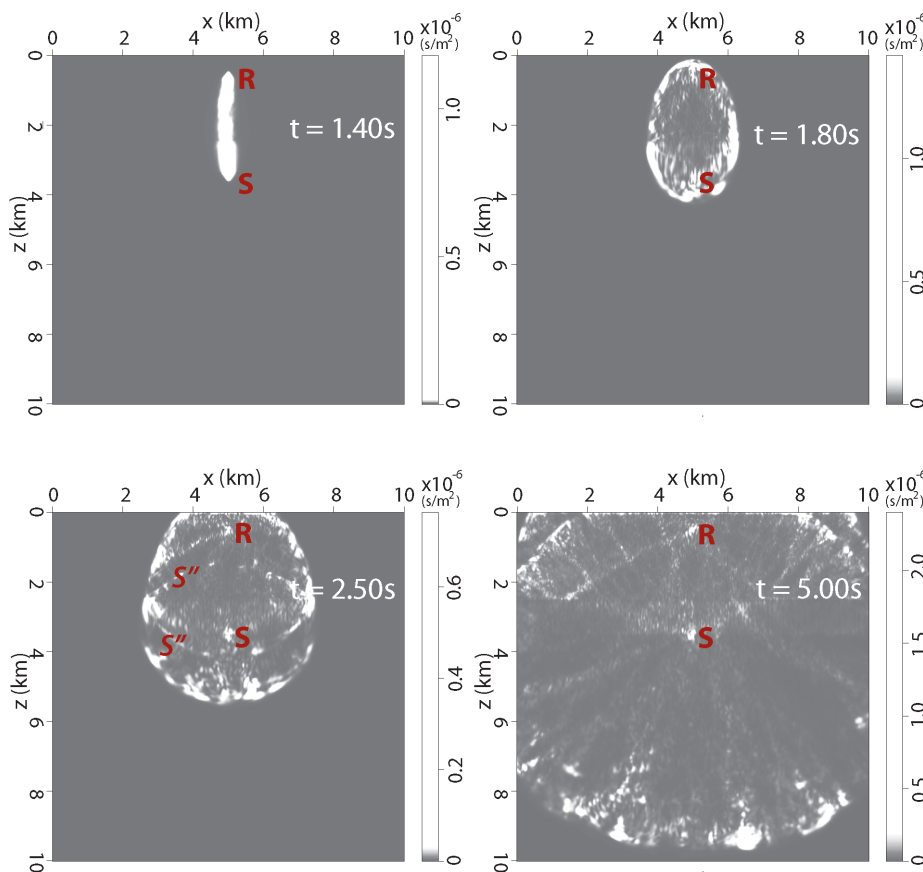


**Figure 9.** Temporal and spatial evolution of the sensitivity kernel (numerical solution) in a reservoir with vertical-fractured-like velocity perturbation with a near-surface receiver.  $S''$  corresponds to the reflected scattered phase.

a receiver at the near surface (for the vertical source–receiver line) or a receiver within a borehole (for the horizontal source–receiver line).

Figs 9 and 10 give snapshots of the sensitivity kernel in the vertically fractured model for the vertical and horizontal source–receiver configurations, respectively. In both source–receiver configurations, the kernels show many of the features present in the kernel of the random isotropic model (Fig. 2), which include the spatial broadening of the kernel with increasing time, the high sensitivity at the source and receiver locations, and the presence of the single scat-

tering contributions to the kernel at the kernel front. However, the heterogeneity in the scattering model introduces extra features to the kernel of the vertically fractured model which are not present in the random isotropic kernel (Fig. 2). In both source–receiver configurations, the width of the kernel (along the minor axes of the kernel) at each layer of the model depends on the effective velocity in that layer (see Figs 9 and 10 at  $t = 2.50$  s). In the vertical source–receiver configuration at  $t = 2.50$  and  $5.00$  s, there are extra scattered fronts marked as  $S''$  within the kernel; these fronts are secondary scattered intensity fronts due to reflections from the layer interfaces

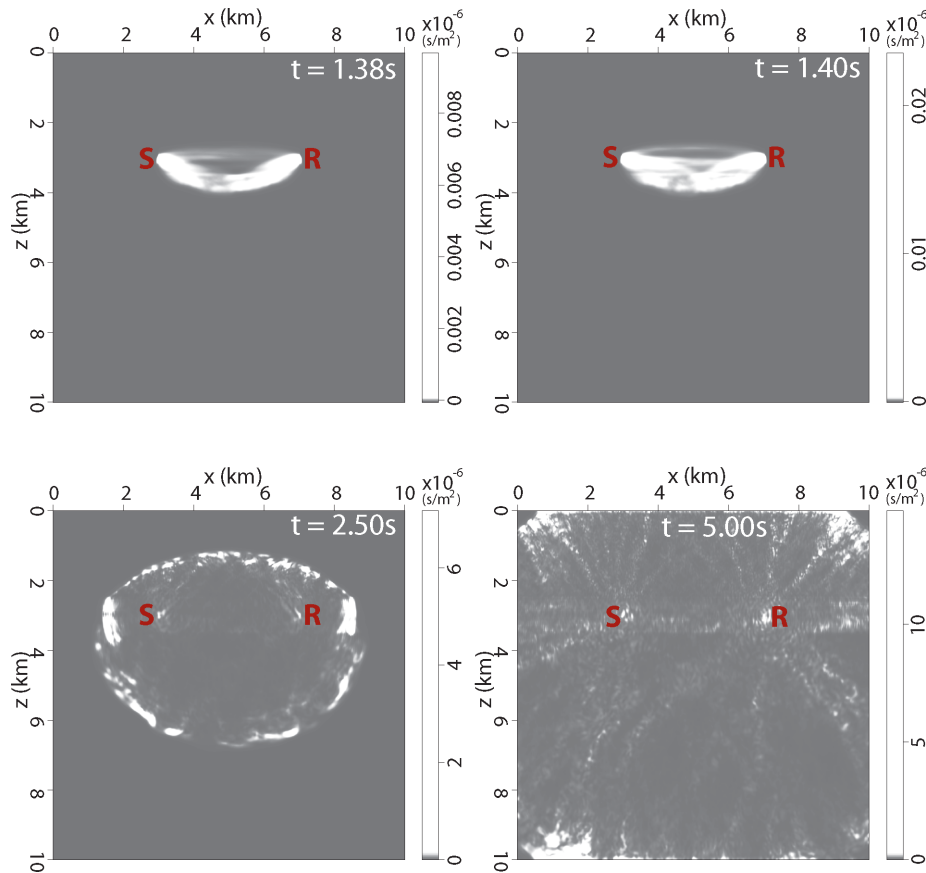


**Figure 10.** Temporal and spatial evolution of the sensitivity kernel (numerical solution) in a reservoir with vertical-fractured-like velocity perturbation with a receiver within the reservoir.

in the model. These reflected fronts lag behind the singly scattered front. In the horizontal source–receiver configuration (Fig. 10), the direct wave refracts through the top interface of the bottom layer because of the higher velocity of the bottom layer (Fig. 10 at  $t = 1.38$  s). A few milliseconds later, many of the forward scattered waves are confined within the middle layer (Fig. 10 at  $t = 1.40$  s). At later lapse times, the singly scattered kernel front propagates out from the middle layer into the top and the bottom layers. The extent of the front propagation depends on the average velocity of the layer. The reflected wave fronts  $S'$  seen in the vertical source–receiver configuration are absent in the kernel with the horizontal source–receiver configuration. This is because the reflectors are parallel to the source–receiver line in the horizontal configuration. The sensitivity is dominant within the middle layer because the vertical velocity perturbations within the middle layer persistently reflect waves propagating horizontally between the source and the receiver. The orientations of the velocity perturbations are perpendicular to the dominant forward propagation of the waves which is along the source–receiver line (Fig. 10 at  $t = 2.50$  and  $5.00$  s). This dominance of the kernel in the middle layer is not present with the vertical source–receiver geometry (Fig. 9), where in the middle layer the wave propagation direction is along the direction of the velocity perturbation. The lack of the kernel dominance within the middle layer with a vertical source–receiver configuration is due to the relative orientation of the source–receiver line and the orientation of the scatterers which results to minimal scattering of the waves compared to the horizontal source–receiver configuration. Also, scattered waves recorded at the receiver have a higher probability of exploring the whole model space without being trapped within middle layer due

to scattering. With the horizontal source–receiver geometry, much of the recorded scattered waves are generated within the middle layer.

Figs 11 and 12 give snapshots of the sensitivity kernel in the shale-like model using the vertical and horizontal source–receiver configurations, respectively. The kernel for the shale-like model, which uses a vertical source–receiver configuration, exhibits similar features present in the vertically fractured model with a similar source–receiver setup. Differences in the kernels are in the multiply scattered part of the kernel in the middle layer of the vertically fractured model where there are elevated scattering close to the source. However, with the horizontal source–receiver configuration (Fig. 12), the kernel at late lapse time ( $t = 2.50$  and  $5.00$  s) shows features different from those present in the kernel with the vertically fractured model using the horizontal source–receiver configuration. The high sensitivity present in the vertically fractured model using the horizontal source–receiver geometry is absent from the model with the horizontal velocity perturbation in the middle layer because the direction of wave propagation between the source and the receiver is parallel to the velocity layering in the middle layer, which results in relatively less scattering of the seismic wave. The effect of the source–receiver configuration on the kernel behaviour implies that the setup of the source and receiver pairs relative to the location of a particular weak change within a scattering medium has large implications for the capability of detecting the weak change. For example, given the relative magnitude of the sensitivities within the middle layer, if there is a change in the middle layer, the horizontal source–receiver geometry provides a better scenario for detecting the weak change in the middle

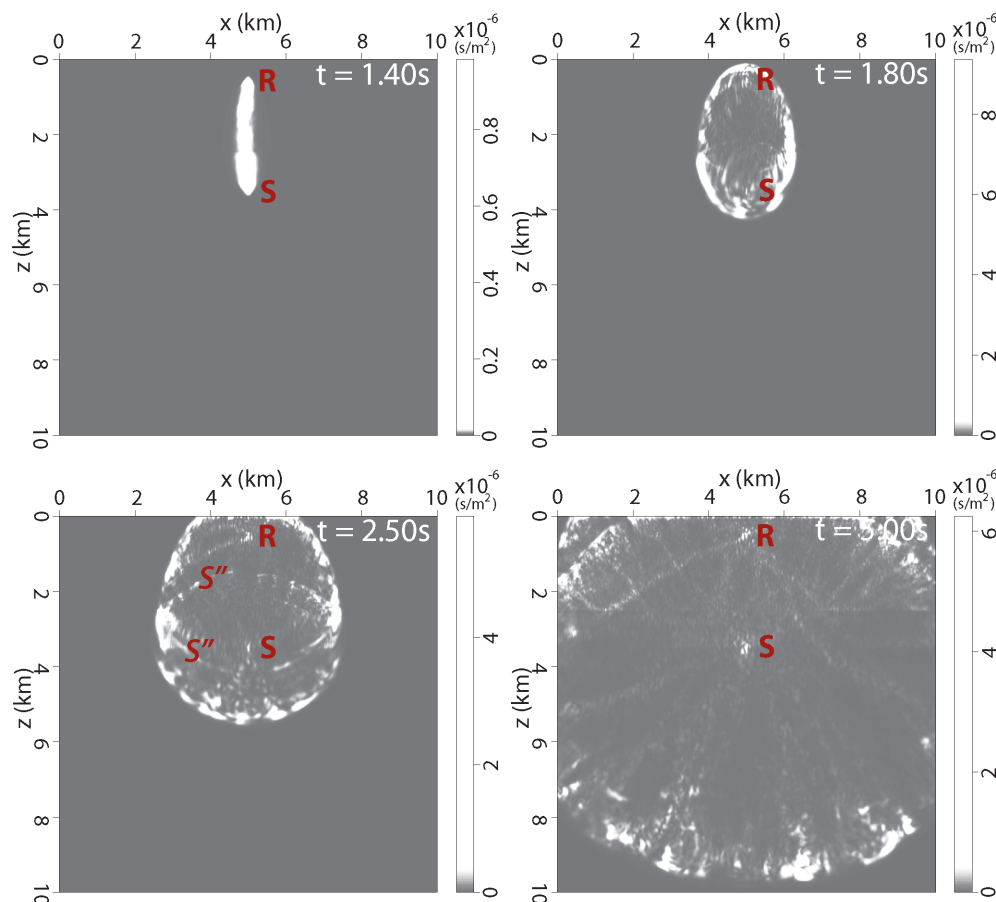


**Figure 11.** Temporal and spatial evolution of the sensitivity kernel (numerical solution) in a reservoir with shale-like velocity perturbation.  $S''$  corresponds to the reflected scattered phase.

layer than the vertical source–receiver geometry. This connection between the source–receiver configuration and the behaviour of the sensitivity kernel suggests the need for the source and receiver to be in close proximity to the location of the weak change. The relative direction of the forward scattering between the source and the receiver to the orientation of the length of the scatterers impacts the relative magnitude of the sensitivity of the scattered intensity to the monitored change. This impact is evident in a comparison of the kernel strength in the middle layers of the vertically fractured model (Fig. 10) to the kernel strength in the middle layer of the shale-like model (Fig. 12). The relative strength of the kernel is higher in the vertically fractured model where the perpendicular alignment of the scatterers allows for a stronger generation of multiply scattered waves.

The kernels at early lapse times are almost identical in both models (Figs 9–12 at  $t = 1.38$  and  $1.40$  s). The kernels at these times consist of mainly direct, refracted, and forward scattered waves.

### 3.3 Topography-induced scattering

Seismic waves are not only scattered by heterogeneities within the earth's subsurface, but also by near-surface heterogeneities such as variable topography or low velocity unconsolidated lithology in the near-surface layers. Due to the high impedance contrast across the free surface and the higher heterogeneities within the near-surface compared to the heterogeneities deeper in the subsurface (Shearer & Earle 2008), the multiple scattering from variable topography and near-surface scattering effects can dominate bulk scattering.

Rough or variable topography plus the presence of the free surface can focus or defocus seismic waves and can convert seismic waves from one wave mode to another such as conversion of body waves to surface waves and vice versa (Levander 1990). Bouchon *et al.* (1996) show that a simple symmetric ridge can induce amplification of a monochromatic  $SH$  wave by up to a factor of 1.5 at the crest of the ridge. The amplification factor of the incident wave depends on the incident angle of the wave and the height to width ratio of the topography perturbation.

To explore the effect of topography on the sensitivity kernel, we simulate an acoustic wavefield using a homogeneous velocity model with a variable topography. The velocity model consists of three homogeneous layers: a top air layer with a velocity of  $330 \text{ m s}^{-1}$ , a thin layer under the topography with a velocity of  $2000 \text{ m s}^{-1}$ , and the rest of the model with a velocity of  $3000 \text{ m s}^{-1}$  (Fig. 13). The free-surface is approximated using the air–subsurface interface based on the velocity discontinuity assuming a constant density (Taillandier *et al.* 2009). We model the variable topography using a 1-D von-Karman PSDF in order to create a random variable topography with a correlation across the topography defined by a correlation distance of  $0.5 \text{ km}$ .

We compute the sensitivity kernel with the scattered waves induced by the variable topography using a vertical source–receiver geometry (Fig. 14) and a horizontal source–receiver configuration (Fig. 15). At time  $t = 1.40$  s, the kernel accounts for the direct wave between source  $S$  and receiver  $R$ . The direct wave kernel using the vertical source–receiver configuration is shown in Fig. 14 at  $t = 1.40$  s. At later lapse time (Fig. 14;  $t > 1.40$  s), the kernel expands

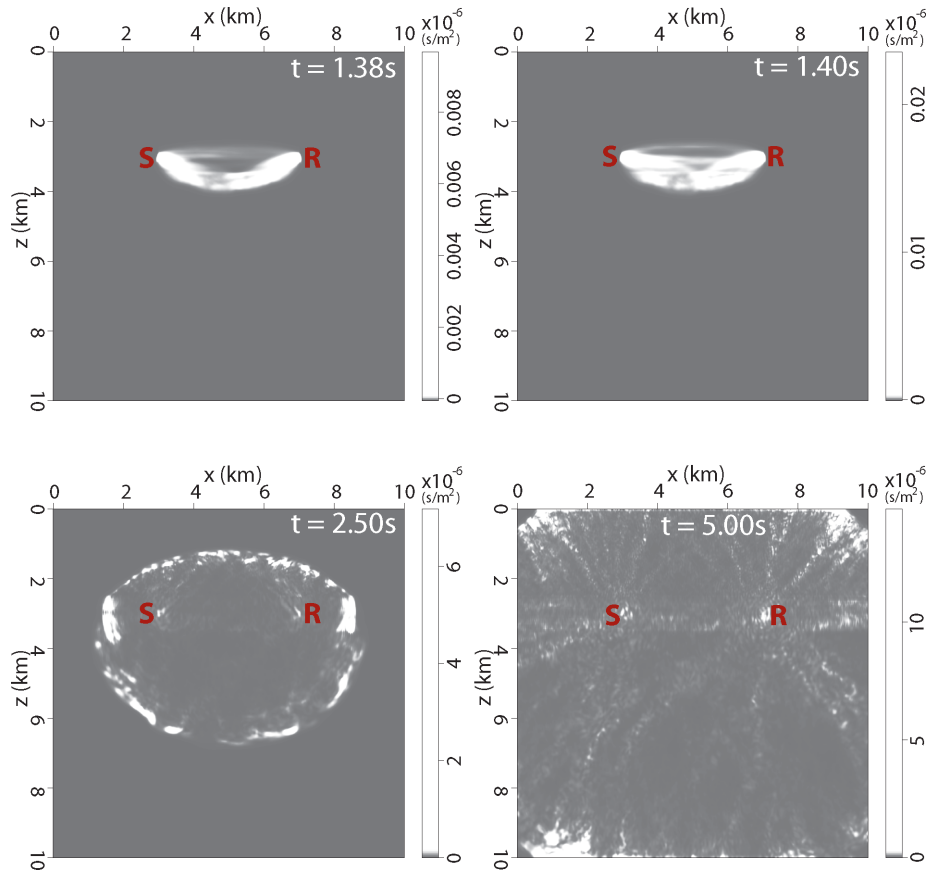


**Figure 12.** Temporal and spatial evolution of the sensitivity kernel (numerical solution) in a reservoir with shale-like velocity perturbation.

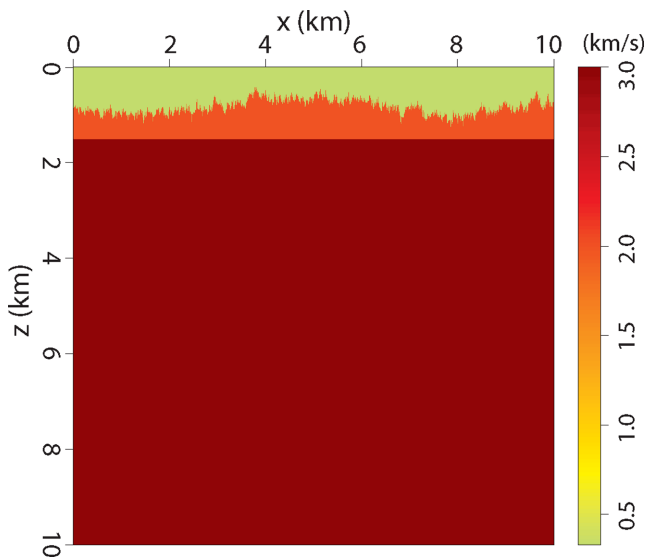


**Figure 13.** Velocity model with variable topography.

into a singly scattered front which broadens with time. The kernel has a relatively large magnitude within the thin low velocity layer underneath the topography (Fig. 14,  $t = 2.5$  and  $5.0$  s). This part of the kernel is due to scattering contributions from the topography-induced scattering which are trapped in the near-surface layer. The topography-induced sensitivity, however, increases and broadens away from the receiver location within the near-surface layer with an increase in time.

When the source and receiver are embedded within the near-surface layer underneath the variable topography, the kernel of the first arrival consists of waves refracted off of the higher velocity half-space underneath the near-surface low velocity layer (Fig. 15,  $t = 1.6$  s). Similar to the vertical source and receiver geometry, the direct/refracted kernel with the horizontal source and receiver setup splits for  $t = 1.8$  s into the singly scattered kernel. In Fig. 15, only the downward section of the singly scattered kernel is present because the high velocity contrast across the topography prevents propagation of scattered waves into the air. At later lapse time ( $t = 2.50$  and  $5.00$  s, Fig. 15), the dominant part of the kernel lies within the low velocity layer which results from the topography-induced scattering and the trapped waves within the low velocity layer. The presence of the thin low velocity layer underneath the topography induces kernels with similar behaviour at large lapse time for both source–receiver configurations.

The behaviour of the kernel in the presence of variable topography and a thin low velocity layer in Figs 14 and 15 demonstrates the need to accurately characterize the scattering properties of the medium being monitored. Incorporating both the topography and the appropriate velocity (scattering) model in the kernel computation provides the distribution and origin of the scattered waves via the kernel that can be used for monitoring weak changes. Due to the effect of variable topography and of a heterogeneous scattering medium on the kernel, we will need to use an appropriate source–receiver array geometry to image a weak change within the subsurface. For example, in a case of monitoring velocity changes within a reservoir that might be due to fluid production or injection within the reservoir, a borehole array in close proximity to the change might be a more effective source–receiver geometry

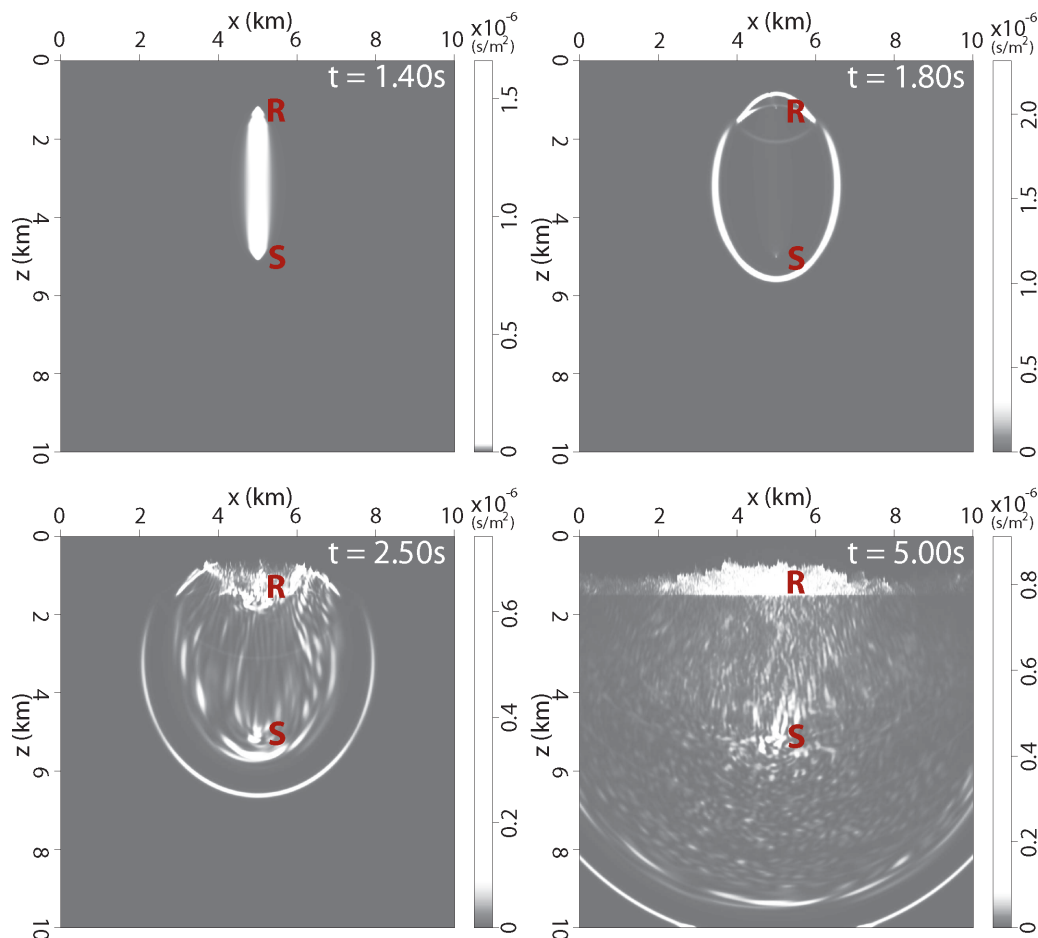


**Figure 14.** Temporal and spatial evolution of the sensitivity kernel (numerical solution) showing topography-induced scattering using vertical source–receiver line.

for monitoring than using a surface–receiver array. In this case, the borehole array records more of the scattered waves generated within a given layer. This results in higher sensitivity to a change in that layer. Also, the borehole array, depending on its relative depth to the free-surface, is less sensitive to waves that are scattered at or near the free surface.

#### 4 DISCUSSION AND CONCLUSION

We propose a novel approach to compute the sensitivity kernel that can be used to resolve weak changes within the earth’s subsurface or any other medium using multiply scattered waves. These are changes which are usually irresolvable with singly scattered waves. Our approach does not rely on analytical models of the scattered intensity such as the diffusion and radiative transfer models. To compute the sensitivity kernel, we compute the intensity field needed for the kernel computation from numerically generated scattered wavefield. In this paper, we use finite-difference modelling for the computation of the seismic wavefield. The numerical modelling of the scattered intensity can take advantage of various numerical methods for seismic wavefield computation. Using our approach we can incorporate any complexities of the scattering medium and any boundary conditions of the medium. With an appropriate *a priori* scattering model, we can obtain a more accurate and detailed estimate of the sensitivity kernel which accurately describes the intensity of the scattered wave recorded by a given source–receiver pair. This numerical estimate of the sensitivity kernel potentially

allows us to resolve a more detailed localized weak changes within a scattering medium compared to changes resolved with kernel which depends on a global estimate of the sensitivity kernel. Our kernel computation approach is suitable for a medium such as the earth’s subsurface where in most cases the scattering properties are heterogeneous and whose scattered intensity may not be described analytically.

The goal for the computation of the sensitivity kernel is to characterize the origin and distribution of the recorded multiply scattered waves use for imaging weak changes within a scattering medium. In Section 3.2.2, the relative orientation of the source–receiver array to the scatterers within a medium affects the distribution and amount of scattered waves generated with the medium, which changes the characteristics of the sensitivity kernel. Imaging of weak changes with a sensitivity kernel that does not embody the local characteristic of the scattering medium especially in statistically complex media might lead to errors in the retrieved velocity changes.

The caveat to the computation of the scattered intensity and in extension the sensitivity kernel for the monitoring weak changes is the computation cost of both the scattered intensity and the corresponding kernel and the need for an accurate *a priori* model of the statistical properties of the scattering medium. The cost of the kernel computation mostly depends on the traveltime of the scattered phase for the kernel, the sum of number of sources and receivers, the number of the scattering model realizations needed, the cost of the forward modelling of the scattered intensity for both the source and receiver intensity fields, and the cost for the convolution

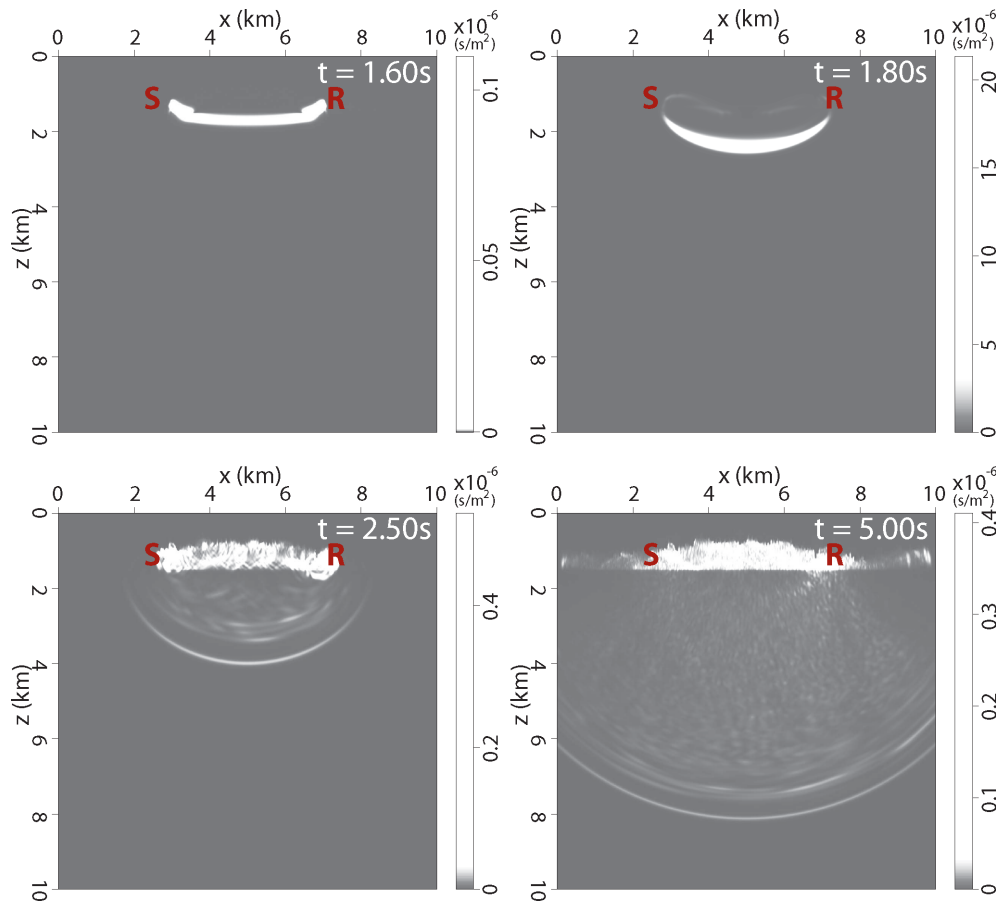


**Figure 15.** Temporal and spatial evolution of the sensitivity kernel (numerical solution) showing topography-induced scattering using horizontal source–receiver line.

between the source and receiver intensity fields. The cost for the forward modelling of the scattered intensity depends on the spatial dimensions of the scattering model used for modelling the intensity field which makes a significant difference if the medium is 2-D or 3-D and the temporal or the frequency dimension of the scattered waves. All numerical examples we show in this paper are based on 2-D models but the computation of the numerical kernel in 3-D follows exactly the same procedure.

Fluctuations in the obtained sensitivity kernels due to speckle caused by the random fluctuations, can be suppressed by averaging the sensitivity kernels over several realizations of the scattering medium. A few realizations of the scattering model (for example, five realizations in the case of homogeneous model in Section 3.2) can significantly stabilize the fluctuations in the sensitivity kernel. However, the amount of realizations needed to reduce the fluctuations to a specified threshold in a given scattering medium depends on the statistical complexity of the scattering medium.

Another limitation of the numerical computation of the sensitivity kernel is the need to know the statistical scattering properties. This limitation is also inherent to the analytical computation of the kernel where the scattering parameter such the diffusion coefficient and the mean free path length are needed for the diffusion and the radiative transfer models, respectively. The details of the scattering model need not be known, as long as it explains the envelope of coda waves, which is an observable quantity, it suffices estimate the sensitivity kernels.

The numerical examples in this study are based on acoustic wave propagation with isotropic source radiation. This acoustic wave as-

sumption can be considered valid at the equipartition regime of multiply scattered waves at which S-wave energy dominates the scattered waves (Weaver 1982; Hennino *et al.* 2001). Equipartitioning of the scattered waves is achieved late in the coda (traveltimes at which diffusion approximation is usually considered). However, our recipe for computing the numerical sensitivity kernel remains valid for elastic wave propagation. For elastic waves, we can compute the sensitivities to the change in *P*- and *S*-wave velocities. The computation of the elastic sensitivity kernels involves additional considerations. Some of these considerations include, separating the *P*- and *S*- wave modes in order to get the sensitivities to *P*- and *S*-wave velocity changes and using the appropriate radiation pattern for the receiver intensity field that depends on the propagation directions of either the recorded *P*- or *S*-wave.

## ACKNOWLEDGEMENTS

This research was supported by sponsors of the Consortium Project on Seismic Inverse Methods for Complex Structures. The reproducible numerical examples in this paper use the Madagascar open-source software package freely available from <http://www.ahay.org>.

## REFERENCES

- Belkebir, K., Chaumet, P.C. & Sentenac, A., 2006. Influence of multiple scattering on three-dimensional imaging with optical diffraction tomography, *J. Opt. Soc. Am. A*, **23**(3), 586–595.

- Berkhout, A., Verschuur, D. & Blacquire, G., 2012. Illumination properties and imaging promises of blended, multiple-scattering seismic data: a tutorial, *Geophys. Prospect.*, **60**(4), 713–732.
- Bouchon, M., Schultz, C.A. & Toksz, M.N., 1996. Effect of three-dimensional topography on seismic motion, *J. geophys. Res.*, **101**(B3), 5835–5846.
- Fleury, C., 2013. Increasing illumination and sensitivity of reverse-time migration with internal multiples, *Geophys. Prospect.*, **61**(5), 891–906.
- Gaburro, R., Nolan, C.J., Dowling, T. & Cheney, M., 2007. Imaging from multiply scattered waves, in *Society of Photo-Optical Instrumentation Engineers*, vol. 6513, pp. 304–311.
- Haney, M.M., van Wijk, K. & Snieder, R., 2005. Radiative transfer in layered media and its connection to the O’Doherty-Anstey formula, *Geophysics*, **70**(1), T1–T11.
- Hennino, R., Trégourès, N., Shapiro, N., Margerin, L., Campillo, M., Van Tiggelen, B. & Weaver, R., 2001. Observation of equipartition of seismic waves, *Phys. Rev. Lett.*, **86**(15), 3447–3450.
- Levander, A.R., 1990. Seismic scattering near the earth’s surface, *Pure appl. Geophys.*, **132**(1–2), 21–47.
- Malcolm, A.E., Ursin, B. & De Hoop, M.V., 2009. Seismic imaging and illumination with internal multiples, *Geophys. J. Int.*, **176**(3), 847–864.
- Margerin, L. & Sato, H., 2011. Reconstruction of multiply-scattered arrivals from the cross-correlation of waves excited by random noise sources in a heterogeneous dissipative medium, *Wave Motion*, **48**(2), 146–160.
- Margerin, L., Campillo, M. & van Tiggelen, B., 1998. Radiative transfer and diffusion of waves in a layered medium: New insight into coda Q, *Geophys. J. Int.*, **134**(2), 596–612.
- Masera, D., Bocca, P. & Grazzini, A., 2011. Frequency analysis of acoustic emission signal to monitor damage evolution in masonry structures, *J. Phys.: Conf. Ser.*, **305**(1), 012134, <http://dx.doi.org/10.1088/1742-6596/305/1/012134>.
- Nishimura, T., Uchida, N., Sato, H., Ohtake, M., Tanaka, S. & Hamaguchi, H., 2000. Temporal changes of the crustal structure associated with the M6.1 earthquake on September 3, 1998, and the volcanic activity of Mount Iwate, Japan, *Geophys. Res. Lett.*, **27**(2), 269–272.
- Obermann, A., Planès, T., Larose, E. & Campillo, M., 2013a. Imaging pre-eruptive and co-eruptive structural and mechanical changes of a volcano with ambient seismic noise, *J. geophys. Res.*, **118**(12), 6285–6294.
- Obermann, A., Planès, T., Larose, E., Sens-Schönfelder, C. & Campillo, M., 2013b. Depth sensitivity of seismic coda waves to velocity perturbations in an elastic heterogeneous medium, *Geophys. J. Int.*, **194**(1), 372–382.
- Paasschens, J.C.J., 1997. Solution of the time-dependent Boltzmann equation, *Phys. Rev. E*, **56**(1), 1135–1141.
- Pacheco, C. & Snieder, R., 2005. Time-lapse travel time change of multiply scattered acoustic waves, *J. acoust. Soc. Am.*, **118**(3), 1300–1310.
- Pacheco, C. & Snieder, R., 2006. Time-lapse traveltimes change of singly scattered acoustic waves, *Geophys. J. Int.*, **165**(2), 485–500.
- Page, J.H., Schriemer, H.P., Bailey, A.E. & Weitz, D.A., 1995. Experimental test of the diffusion approximation for multiply scattered sound, *Phys. Rev. E*, **52**(3), 3106–3114.
- Planès, T., Larose, E., Margerin, L., Rossetto, V. & Sens-Schönfelder, C., 2014. Decorrelation and phase-shift of coda waves induced by local changes: multiple scattering approach and numerical validation, in *Waves in Random and Complex Media*, pp. 1–27, doi:10.1080/17455030.2014.880821.
- Poupinet, G., Ellsworth, W.L. & Frechet, J., 1984. Monitoring velocity variations in the crust using earthquake doublets: an application to the Calaveras fault, California, *J. geophys. Res.*, **89**(B7), 5719–5731.
- Ripoll, J., Nieto-Vesperinas, M. & Arridge, S.R., 2001. Effect of roughness in nondiffusive regions within diffusive media, *J. Opt. Soc. Am. A*, **18**(4), 940–947.
- Rossetto, V., Margerin, L., Planès, T. & Larose, E., 2011. Locating a weak change using diffuse waves: Theoretical approach and inversion procedure, *J. Appl. Phys.*, **109**(3), 903–911.
- Sato, H., Fehler, M.C. & Maeda, T., 2012. *Seismic Wave Propagation and Scattering in the Heterogeneous Earth: Second Edition*, Springer.
- Schaff, D.P. & Beroza, G.C., 2004. Coseismic and postseismic velocity changes measured by repeating earthquakes, *J. geophys. Res.*, **109**(B10), B10302, doi:10.1029/2004JB003011.
- Shapiro, S.A. & Kneib, G., 1993. Seismic attenuation by scattering: theory and numerical results, *Geophys. J. Int.*, **114**(2), 373–391.
- Shearer, P.M. & Earle, P.S., 2008. Observing and modeling elastic scattering in the deep earth, *Adv. Geophys.*, **50**, 167–194.
- Snieder, R., 2002. Coda wave interferometry and the equilibration of energy in elastic media, *Phys. Rev. E*, **66**(4), 046615.
- Snieder, R., Grêt, A., Douma, H. & Scales, J., 2002. Coda wave interferometry for estimating nonlinear behavior in seismic velocity, *Science*, **295**, 2253–2255.
- Taillandier, C., Noble, M., Chauris, H. & Calandra, H., 2009. First-arrival traveltimes tomography based on the adjoint-state method, *Geophysics*, **74**(6), WCB1–WCB10.
- Turner, J.A. & Weaver, R.L., 1994. Radiative transfer and multiple scattering of diffuse ultrasound in polycrystalline media, *The J. acoust. Soc. Am.*, **96**(6), 3675–3683.
- Vlastos, S., Liu, E., Main, I.G., Schoenberg, M., Narteau, C., Li, X.Y. & Maillot, B., 2006. Dual simulations of fluid flow and seismic wave propagation in a fractured network: Effects of pore pressure on seismic signature, *Geophys. J. Int.*, **166**(2), 825–838.
- Weaver, R., 1982. On diffuse waves in solid media, *J. acoust. Soc. Am.*, **71**, 1608–1609.
- Wegler, U. & Sens-Schönfelder, C., 2007. Fault zone monitoring with passive image interferometry, *Geophys. J. Int.*, **168**(3), 1029–1033.
- Wesley, J.P., 1965. Diffusion of seismic energy in the near range, *J. geophys. Res.*, **70**(20), 5099–5106.
- Yodh, A. & Chance, B., 1995. Spectroscopy and imaging with diffusing light, *Phys. Today*, **48**(3), 34–41.
- Yoshimoto, K. & Sato, H., 1997. Short-wavelength crustal heterogeneities in the Nikko area, Central Japan, revealed from the three-component seismogram envelope analysis, *Phys. Earth planet. Inter.*, **104**(1), 63–73.